



Neural network-based time optimal trajectory planning method for rotary cranes with obstacle avoidance

Hongjie Zhu, Huimin Ouyang, Huan Xi *

College of Electrical Engineering and Control Science, Nanjing Tech University, No. 30, Puzhu Road(s), Nanjing, 211816, China

ARTICLE INFO

Communicated by X. Jing

Keywords:

Rotary crane
Motion control
Trajectory planning
Neural network
Obstacles avoidance

ABSTRACT

In this paper, an improved trajectory planning method is proposed, which can effectively avoid obstacles on the path and control the swing of the load during the transportation of a rotating crane within a certain range. The complex dynamics model of the rotary crane is first analyzed, and then the system constraint equations are established to ensure the transient performance during the boom motion. And an optimal time trajectory is obtained by the dichotomy method. Then, the trajectories for different obstacles, different starting positions and different final positions are generated by combining with a neural network method to achieve different control requirements. Finally, to confirm the superiority of the proposed method, it is verified by a hardware experimental platform.

1. Introduction

Rotary cranes have the advantages of high mobility, low cost and wide application environment. They play a vital role in the transportation industry. However, most of them are still operated by manual operation, which inevitably lead to a series of problems. For example, the total duration of manual operation is uncertain. And it is difficult to control the time to eliminate load swing by manual operation. These significantly reduce the operational efficiency of the rotating crane system. In addition, even skilled operators are inevitably subject to safety problems [1]. The rotary crane system has strong nonlinear dynamic coupling characteristics, and its control problems are more complex than most underactuated systems.

Therefore, many scholars have proposed various automatic control methods for rotary cranes while studying the above-mentioned problems. These include adaptive control method [2–5], sliding mode control method [6–9], energy coupling control method [10–12], optimal control [13–17], intelligent algorithms [18–20], input shaping [21–24], etc. Because the rotary crane will generate complex centrifugal forces on the load when rotating and lifting, which makes the load oscillate significantly. Therefore, it is difficult to ensure the dynamic performance of the underactuated variables. In addition, the dynamics model of rotary crane system has a complex coupling between state variables, making the controller design task more onerous.

The most important objectives of a rotary crane system are boom positioning and load swing elimination. Ouyang et al. [25] proposed an energy-shaping-based control method for rotary cranes, in which the gain of the controller is selected within a certain range. The method is able to limit the output of the controller, which will not make the drive motor damaged and also enable accurate positioning of the boom and excellent swing elimination function. In [26], an adaptive control method was proposed based on the dynamics model with parameter variation, which can effectively compensate the frictional force during the operation of the rotary crane. By analyzing the complex nonlinear dynamic coupling characteristics of the rotary crane, Yang Tong et al. proposed a new nonlinear time optimal trajectory planning method [27]. And it does not require linearization of the system

* Corresponding author.

E-mail address: huanxinjtech@163.com (H. Xi).

dynamics equations and achieves the diverse control objectives of the rotary crane with single pendulum performance by establishing state constraint equations and other means. There are many intelligent algorithms that have been applied in the control design of rotary cranes [28]. In addition, the adaptive output feedback control method proposed in [29] achieves accurate motion control and time-varying constraints for all variables. Also this method has good application value and theoretical value. In [30], a new adaptive optimal controller is designed for a class of under-driven electromechanical systems with model uncertainty and actuator saturation. The neuroadaptive controller proposed in [31] solves both driven and undriven output/speed constraints for a class of MIMO uncertain and under-driven systems. A target ship motion prediction algorithm is proposed in [32], which can predict/update the target ship motion trajectory online and greatly alleviate the requirement for accurate track information. In the presence of unknown disturbances, the programming-based optimal learning sliding mode control strategy proposed in [33] is able to suppress the mismatch interference well.

For the real situation of rotary crane operation, it is inevitable that there are obstacles in the scene. Then the obstacles avoidance issue should be considered. For instance, during crane transportation in a port, there are many containers in the fixed area, which makes the movement of the crane limited. A time-optimal trajectory planning method for obstacle avoidance was proposed, which is applied to the overhead crane system [34]. Although this method can reduce the computation time by checking the table, there are limitations to the real-time implementation of the optimal trajectory. Therefore, this paper investigates an optimal time trajectory planning method for obstacle avoidance for a rotary crane system with certain robustness to system parameter changes. And an adaptive mechanism that can update the trajectory parameters in real time was incorporated. The experimental results showed that the neural network architecture trained by the training set can predict the parameters for different obstacle trajectories well to achieve the control requirements of obstacle avoidance, boom positioning, and load dissipation. In general, the advantages of the method proposed in this paper are as follows:

1. The dynamics model of a rotary crane is used as a starting point to analyze the coupling relationship between state variables in a complex nonlinear system. And the swing angle of the load is used to represent the rotation and heave angles. As a result, the trajectory planning problem of the boom motion is converted into the trajectory planning problem of the state variables mentioned above. On this basis, the constraint equations are established. Next, the trajectory of optimal time is obtained by calculating the constraint equations through the dichotomy idea. During the analysis, no linearization of the system equations is performed. Even if the state variables are larger away from the equilibrium position, the proposed optimal time trajectory can still achieve the control objectives of obstacle avoidance, positioning, and pendulum elimination.
2. The proposed control method can adapt to different control requirements by setting the trajectory according to different obstacle positions, different starting positions and different final positions to get the optimal time trajectory for obstacle avoidance in real time. In addition, the trajectories can be planned according to different physical constraints, which ensures the transient performance of the system.
3. A comparison with existing methods was made on an experimental platform of a rotary crane with single pendulum characteristics. The validity of the proposed method was verified.

The rest of the paper is organized as follows. The dynamics model of the rotary crane is given in Section 2. Then, the nonlinear relationship between the state variables and the coordinate signals is analyzed to design the obstacle avoidance trajectory. Next, the analysis is performed for the position of the obstacles. The time optimal problem is solved by the idea of dichotomy, which provides the training set for the neural network. The third section deals with the performance analysis of the neural network. The fourth section demonstrates the superior performance of the proposed method through experiments. The final section summarizes the content of this paper and describes considerations for future.

2. Problem statement

2.1. Model establishment

As shown in Fig. 1, the dynamic equations of the rotary crane in the inertial coordinate system are as follows [35]:

$$ml^2(1 + \xi_1^2)\ddot{\xi}_1 + ml^2\xi_1\xi_2\ddot{\xi}_2 + mlL(-\xi_1S_3 + C_3)\ddot{\xi}_3 - ml^2\xi_2\ddot{\xi}_4 + ml^2\xi_1(\ddot{\xi}_1^2 + \ddot{\xi}_2^2) - mlL(S_3 + \xi_1C_3)\ddot{\xi}_3^2 - ml(l\xi_1 + LS_3)\ddot{\xi}_4^2 - 2ml^2\xi_2\ddot{\xi}_4 + mgl\xi_1 = \tau_1 - \tau_{1f} \quad (1)$$

$$ml^2\xi_1\xi_2\ddot{\xi}_1 + ml^2(1 + \xi_2^2)\ddot{\xi}_2 - mlL\xi_2S_3\ddot{\xi}_3 + (ml^2\xi_1 + mlLS_3)\ddot{\xi}_4 + ml^2\xi_2(\ddot{\xi}_1^2 + \ddot{\xi}_2^2) - mlL\xi_2C_3\ddot{\xi}_3^2 - ml^2\xi_2\ddot{\xi}_4^2 + 2ml^2\xi_1\ddot{\xi}_4 + 2mlL\xi_3\ddot{\xi}_4C_3 + mgl\xi_2 = \tau_2 - \tau_{2f} \quad (2)$$

$$mlL(C_3 - \xi_1S_3)\ddot{\xi}_1 - mlL\xi_2S_3\ddot{\xi}_2 + (mL^2 + J_y)\ddot{\xi}_3 - mlL\xi_2C_3\ddot{\xi}_4 - mlLS_3(\ddot{\xi}_1^2 + \ddot{\xi}_2^2) - 2mlL\xi_2\ddot{\xi}_4C_3 - g\left(\frac{1}{2}M_lL + mL - \frac{1}{2}M_lL_1\right)S_3 - \left(\frac{1}{2}(J_x - J_z)\sin(2\xi_3) + mlL\xi_1C_3 + \frac{1}{2}mL^2\sin(2\xi_3)\right)\ddot{\xi}_4^2 = \tau_3 - \tau_{3f} \quad (3)$$

$$-ml^2\xi_2\ddot{\xi}_1 + (ml^2\xi_1 + mlLS_3)\ddot{\xi}_2 - mlL\xi_2C_3\ddot{\xi}_3 + mlL\xi_2\ddot{\xi}_3^2S_3 + (mL^2\xi_3\sin(2\xi_3) + 2ml^2(\xi_1\ddot{\xi}_1 + \xi_2\ddot{\xi}_2) + 2mlL(\xi_1S_3 + \xi_1\xi_3C_3) + (J_x - J_z)\ddot{\xi}_3\sin(2\xi_3))\ddot{\xi}_4 + (mL^2S_3^2 + ml^2(\xi_1^2 + \xi_2^2) + 2mlL\xi_1S_3 + I_b + J_xS_3^2 + J_zC_3^2)\ddot{\xi}_4 = \tau_4 - \tau_{4f} \quad (4)$$

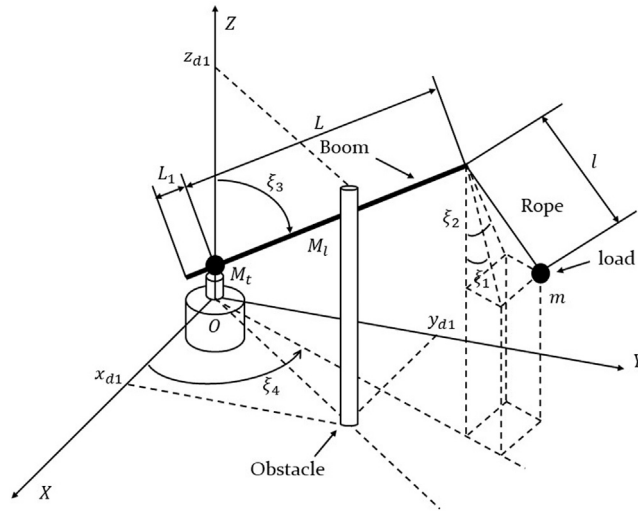


Fig. 1. Rotary crane model with an obstacle.

Table 1

Meaning for parameters of the rotary crane system.

Parameters	Physical	Units
$\xi_1(t)$	Rope radial sway angle	rad
$\xi_2(t)$	Rope tangential sway angle	rad
$\xi_3(t)$	Load radial sway angle	rad
$\xi_4(t)$	Load tangential sway angle	rad
M_l	Boom mass	kg
M_b	Ballast mass	kg
m	Load mass	kg
L	Boom length	m
L_1	Ballast length	m
l	Rope length	m
J_x, J_y, J_z	Moments of inertia of the boom	kg m ²
I_b	Ballast inertia moment	kg m ²
$f_{31}, f_{32}, f_{41}, f_{42}, \epsilon$	Friction related quantity	–

where

$$\tau_{1f} = 0, \tau_{2f} = 0, \tau_{3f} = f_{31} \tanh\left(\frac{\dot{\xi}_3}{\epsilon}\right) + f_{32} |\dot{\xi}_3| \dot{\xi}_3, \tau_{4f} = f_{41} \tanh\left(\frac{\dot{\xi}_4}{\epsilon}\right) + f_{42} |\dot{\xi}_4| \dot{\xi}_4, \tau_1 = 0, \tau_2 = 0.$$

It is necessary to clarify that τ_i is the input force, τ_{if} ($i = 1, 2, 3, 4$) is the friction force to be overcome. $f_{31}, f_{32}, f_{41}, f_{42}$ and ϵ are friction coefficients and the values of ϵ can be identified by abundant advanced off-line experiments and data fitting [3,5,9,11,25]. In this paper, the obstacle is seen as a long, thin rod. (x_{d1}, y_{d1}, z_{d1}) is the 3D coordinate of the obstacle. All other parameters in the dynamical system model are defined in Table 1. In addition, to make the expression of the system model more intuitive, $\cos \xi_3$ and $\sin \xi_4$ are replaced with C_3 and S_4 , respectively. In addition, considering the actual operation of the crane and the convenience of the algorithm design, the following assumptions are made for the crane system [2,3,10,12,25,35].

- The rope can be seen as massless rigid link, and its flexibility and torsion can be neglected.
- For cranes working in practice, the payload is always beneath the boom. Hence, the load sway angles always satisfy:

$$\xi_i \in \left(-\frac{\pi}{2}, \frac{\pi}{2}\right), i = 1, \dots, 4.$$

2.2. Trajectory planning

By analyzing the coordinate relationships in Fig. 1, the coordinates at the end of the boom of the rotary crane can be obtained.

$$\begin{aligned} x_0 &= L \sin \xi_3 \cos \xi_4 \\ y_0 &= L \sin \xi_3 \sin \xi_4 \\ z_0 &= L \cos \xi_3 \end{aligned}$$

(5)

Similarly, the load coordinates below the boom are as follows:

$$x = L \sin \xi_3 \cos \xi_4 + l \xi_1 \cos \xi_4 - l \xi_2 \sin \xi_4 \quad (6)$$

$$y = L \sin \xi_3 \sin \xi_4 + l \xi_1 \sin \xi_4 + l \xi_2 \cos \xi_4 \quad (7)$$

$$z = L \cos \xi_3 - l \cos(\sqrt{\xi_1^2 + \xi_2^2}) \quad (8)$$

After deriving Eqs. (6)–(8) twice, the following results are obtained:

$$\begin{aligned} \ddot{x} = & L \ddot{\xi}_3 C_3 C_4 - L \ddot{\xi}_4 S_3 S_4 - L \dot{\xi}_3^2 S_3 C_4 - L \dot{\xi}_4^2 S_3 C_4 \\ & - 2L \dot{\xi}_3 \dot{\xi}_4 C_3 S_4 + l \ddot{\xi}_1 C_4 - l \ddot{\xi}_2 S_4 - 2l \dot{\xi}_1 \dot{\xi}_4 S_4 \\ & - 2l \dot{\xi}_2 \dot{\xi}_4 C_4 - l \xi_1 \ddot{\xi}_4 S_4 - l \xi_1 \dot{\xi}_4^2 C_4 - l \xi_2 \ddot{\xi}_4 C_4 \\ & + l \xi_2 \dot{\xi}_4^2 S_4 \end{aligned} \quad (9)$$

$$\begin{aligned} \ddot{y} = & L \ddot{\xi}_3 C_3 S_4 + L \ddot{\xi}_4 S_3 C_4 - L \dot{\xi}_3^2 S_3 S_4 - L \dot{\xi}_4^2 S_3 S_4 \\ & + 2L \dot{\xi}_3 \dot{\xi}_4 C_3 C_4 + l \ddot{\xi}_1 S_4 + l \ddot{\xi}_2 C_4 + 2l \dot{\xi}_1 \dot{\xi}_4 C_4 \\ & - 2l \dot{\xi}_2 \dot{\xi}_4 S_4 + l \xi_1 \ddot{\xi}_4 C_4 - l \xi_1 \dot{\xi}_4^2 S_4 - l \xi_2 \ddot{\xi}_4 S_4 \\ & - l \xi_2 \dot{\xi}_4^2 C_4 \end{aligned} \quad (10)$$

$$\ddot{z} = -L \ddot{\xi}_3 S_3 - L \dot{\xi}_3^2 C_3 + l \ddot{\xi}_1 + l \xi_1 \ddot{\xi}_1 + l \xi_2^2 + l \xi_2 \ddot{\xi}_2 \quad (11)$$

The above expressions are processed to obtain the following equations:

$$\begin{aligned} \ddot{x} C_4 + \ddot{y} S_4 = & L \ddot{\xi}_3 C_3 - L \dot{\xi}_3^2 - L \dot{\xi}_4^2 S_3 \\ & + l \ddot{\xi}_1 - 2l \dot{\xi}_2 \dot{\xi}_4 - l \xi_1 \dot{\xi}_4^2 - l \xi_2 \ddot{\xi}_4 \end{aligned} \quad (12)$$

$$\begin{aligned} \ddot{x} S_4 - \ddot{y} C_4 = & -L \ddot{\xi}_4 S_3 - l \ddot{\xi}_2 - 2l \dot{\xi}_1 \dot{\xi}_4 \\ & - l \xi_1 \ddot{\xi}_4 + l \xi_2 \dot{\xi}_4^2 - 2L \dot{\xi}_3 \dot{\xi}_4 C_3 \end{aligned} \quad (13)$$

Eq. (11) is multiplied by ξ_1 and ξ_2 to obtain the following equations:

$$\begin{aligned} \xi_1 \ddot{z} = & -L \xi_1 \ddot{\xi}_3 S_3 - L \xi_1 \dot{\xi}_3^2 C_3 + l \xi_1 \ddot{\xi}_1 + l \xi_1^2 \ddot{\xi}_1 \\ & + l \xi_1 \dot{\xi}_2^2 + l \xi_1 \xi_2 \ddot{\xi}_2 \end{aligned} \quad (14)$$

$$\begin{aligned} \xi_2 \ddot{z} = & -L \xi_2 \ddot{\xi}_3 S_3 - L \xi_2 \dot{\xi}_3^2 C_3 + l \xi_2 \dot{\xi}_1^2 + l \xi_1 \xi_2 \ddot{\xi}_1 \\ & + l \xi_2 \dot{\xi}_2^2 + l \xi_2^2 \ddot{\xi}_2 \end{aligned} \quad (15)$$

Then, substituting Eqs. (14) and (15) into Eqs. (1) and (2), we have

$$l \ddot{\xi}_1 - l \xi_2 \ddot{\xi}_4 + L \ddot{\xi}_3 C_1 - L \dot{\xi}_3^2 S_3 - l \xi_1 \dot{\xi}_4^2 - L \dot{\xi}_4^2 S_3 - 2l \dot{\xi}_2 \dot{\xi}_4 + \xi_1 \ddot{z} + g \xi_1 = 0 \quad (16)$$

$$l \ddot{\xi}_2 - l \xi_1 \ddot{\xi}_4 + L \ddot{\xi}_4 S_3 - l \xi_4^2 \xi_2 + 2l \dot{\xi}_1 \dot{\xi}_4 + 2L \dot{\xi}_3 \dot{\xi}_4 C_1 + \xi_2 \ddot{z} + g \xi_2 = 0 \quad (17)$$

Substituting Eqs. (16) and (17) into Eqs. (12) and (13), the following expression can be obtained:

$$\ddot{x} C_4 + \ddot{y} S_4 = -\xi_1 \ddot{z} - g \xi_1 \quad (18)$$

$$\ddot{x} S_4 - \ddot{y} C_4 = \xi_2 \ddot{z} + g \xi_2 \quad (19)$$

The pendulum angle signals can be obtained from the coordinate deformation of the load, and the following results can be obtained from Eqs. (6) and (7).

$$\xi_1 = \frac{(y S_4 + x C_4 - L S_3)}{l} \quad (20)$$

$$\xi_2 = \frac{(y C_4 - x S_4)}{l} \quad (21)$$

Eq. (18) is multiplied by $\cos \xi_4$ and Eq. (19) is multiplied by $\sin \xi_4$, and then the results are added together. Finally, Eqs. (20)–(21) are substituted to derive the expressions below.

$$\begin{aligned} \ddot{x} C_4^2 + \ddot{x} S_4^2 = & -\frac{(\ddot{z} + g)(x S_4^2 + x C_4^2)}{l} + \frac{L S_3 C_4 (\ddot{z} + g)}{l} \\ \Rightarrow & \frac{\ddot{z} + g}{l} x + \ddot{x} = \frac{\ddot{z} + g}{l} L S_3 C_4 \\ \Rightarrow & \left(\frac{\ddot{z} + g}{l} x + \ddot{x} \right) \tan(\xi_4) = \frac{\ddot{z} + g}{l} y_0 \\ \Rightarrow & \xi_4 = \arctan \partial \end{aligned} \quad (22)$$

where

$$\partial = \frac{y_0}{x + \frac{l\ddot{x}}{g+z}}$$

Substituting Eq. (22) into the expression for y_0 in Eq. (5) yields,

$$\xi_3 = \arcsin\left(\frac{y_0}{L \sin(\xi_4)}\right) \quad (23)$$

Substituting Eqs. (22) and (23) into Eqs. (20) and (21) yields,

$$\xi_1 = \frac{(y \sin(\arctan \partial) + x \cos(\arctan \partial) - \frac{y_0}{L \sin(\arctan \partial)})}{l} \quad (24)$$

$$\xi_2 = \frac{(y \cos(\arctan \partial) - x \sin(\arctan \partial))}{l} \quad (25)$$

From all the results obtained above, it can be seen that the state variables of the rotary crane system can be represented by the coordinate values of x, y, z, y_0 . Next, the corresponding constraint equations are set to design the trajectory that satisfies the control requirements. Finally the solution of solving the constraint equations is transformed into the problem of optimization.

2.3. Optimization problem construction

In this subsection, the optimal time trajectory for obstacle avoidance is designed by constraint equations satisfied by the coordinate values. During the operation of the rotary crane with the trajectory, we consider the terminal coordinates of the boom to be higher than the coordinates of the highest point of the obstacle (i.e., the load z -axis coordinates reach the apex of the obstacle) to achieve the obstacle avoidance function at the moment t_s . Then, the swing of the load is also satisfied to be zero at the end moment T_F . At this point, the boom has crossed the obstacle from the initial position to the desired final position. And the constraint equations are set as follows:

$$\begin{aligned} x(0) &= x_{d0}, x^{(i)}(0) = 0, x(t_s) = x_{d1}, x^{(i)}(t_s) = 0, x(T_F) = x_d, x^{(i)}(T_F) = 0 \\ y(0) &= y_{d0}, y^{(i)}(0) = 0, y(t_s) = y_{d1}, y^{(i)}(t_s) = 0, y(T_F) = y_d, y^{(i)}(T_F) = 0 \\ z(0) &= z_{d0}, z^{(i)}(0) = 0, z(t_s) = z_{d1}, z^{(i)}(t_s) = 0, z(T_F) = z_d, z^{(i)}(T_F) = 0 \\ y_0(0) &= y_{0d0}, y_0^{(j)}(0) = 0, y_0(T_F) = y_{0d}, y_0^{(j)}(T_F) = 0 \\ i &= 1, 2, 3, 4, j = 1, 2, 3 \end{aligned} \quad (26)$$

where x_{d0}, y_{d0} and z_{d0} are the starting coordinates of the load, and y_{0d0} is the starting coordinate value of the y -axis direction at the end of the cantilever. Similarly, y_{0d} is the final position. x_{d1}, y_{d1} and z_{d1} are the coordinate values of the obstacle in the 3D coordinate system. x_d, y_d and z_d are the final positions of the load movement.

In the whole transporting obstacle avoidance process, the speed and acceleration of the longitudinal coordinates of the end of the boom and the load coordinates should meet different control requirements. And they should all be within the appropriate range to ensure the safety performance. In view of the restrictions, they should be satisfied on the undulation and rotation angle acceleration signals. And they are related to the fourth order derivatives of x, y, z, y_0 . This is the reason for the restriction to its fourth order derivative.

$$\begin{aligned} |\dot{x}| &\leq v_{1\max}, |\dot{y}| \leq v_{2\max}, |\dot{z}| \leq v_{3\max}, |\dot{y}_0| \leq v_{4\max} \\ |\ddot{x}| &\leq a_{1\max}, |\ddot{y}| \leq a_{2\max}, |\ddot{z}| \leq a_{3\max}, |\ddot{y}_0| \leq a_{4\max} \\ |x^{(3)}| &\leq j_{1\max}, |y^{(3)}| \leq j_{2\max}, |z^{(3)}| \leq j_{3\max}, |y_0^{(3)}| \leq j_{4\max} \\ |\xi_1| &\leq \xi_{1\max}, |\xi_2| \leq \xi_{2\max} \\ |\dot{\xi}_1| &\leq w_{1\max}, |\dot{\xi}_2| \leq w_{2\max}, |\dot{\xi}_3| \leq w_{3\max}, |\dot{\xi}_4| \leq w_{4\max} \\ |\ddot{\xi}_3| &\leq a_{\alpha\max}, |\ddot{\xi}_4| \leq a_{\beta\max} \end{aligned} \quad (27)$$

where $v_{p\max}, a_{p\max}$ and $j_{p\max}, p = 1, 2, 3, 4$ are the velocity, acceleration and jerk constraints on the coordinates. $\xi_{1\max}$ and $\xi_{2\max}$ denote the maximum amplitude of the load tangential and radial oscillations, respectively. $w_{1\max}$ and $w_{2\max}$ are limits on the speed of the load swing angle. $w_{3,4\max}$ and $a_{\alpha,\beta\max}$ are the velocity and acceleration constraints on the boom undulation and rotation angles.

According to the constraint equations, we choose to use a curve of 9th order polynomial to parameterize the 3D coordinate signal of the load with the following expressions:

$$x(t) = \begin{cases} (x_{d1} - x_{d0}) \sum_{i=1}^9 \chi_i \left(\frac{t}{T_F}\right)^i + x_{d0}, t \in [0, t_s] \\ (x_d - x_{d1}) \sum_{i=1}^9 \chi_i \left(\frac{t}{T_F}\right)^i + x_{d1}, t \in [t_s, T_F] \end{cases}$$

$$\begin{aligned}
y(t) &= \begin{cases} (y_{d1} - y_{d0}) \sum_{i=1}^9 \chi_i \left(\frac{t}{T_F}\right)^i + y_{d0}, t \in [0, t_s) \\ (y_d - y_{d1}) \sum_{i=1}^9 \chi_i \left(\frac{t}{T_F}\right)^i + y_{d1}, t \in [t_s, T_F] \end{cases} \\
z(t) &= \begin{cases} (z_{d1} - z_{d0}) \sum_{i=1}^9 \chi_i \left(\frac{t}{T_F}\right)^i + z_{d0}, t \in [0, t_s) \\ (z_d - z_{d1}) \sum_{i=1}^9 \chi_i \left(\frac{t}{T_F}\right)^i + z_{d1}, t \in [t_s, T_F] \end{cases}
\end{aligned} \quad (28)$$

Similarly, the expression for the y -axis signal at the end of the boom can be obtained.

$$y_0(t) = y_{0d0} + (y_{0d} - y_{0d0}) \sum_{i=1}^7 \psi_i \left(\frac{t}{T_F}\right)^i, t \in [0, T_F] \quad (29)$$

The form of the derivative of the designed curves are as follows:

$$\begin{aligned}
x^{(k)}(t) &= \begin{cases} (x_{d1} - x_{d0}) \sum_{i=5}^9 \chi_i \frac{i!}{(i-k)!} \left(\frac{1}{T}\right)^i t^{i-k}, t \in [0, t_s) \\ (x_d - x_{d1}) \sum_{i=5}^9 \chi_i \frac{i!}{(i-k)!} \left(\frac{1}{T}\right)^i t^{i-k}, t \in [t_s, T_F] \end{cases} \\
y^{(k)}(t) &= \begin{cases} (y_{d1} - y_{d0}) \sum_{i=5}^9 \chi_i \frac{i!}{(i-k)!} \left(\frac{1}{T}\right)^i t^{i-k}, t \in [0, t_s) \\ (y_d - y_{d1}) \sum_{i=5}^9 \chi_i \frac{i!}{(i-k)!} \left(\frac{1}{T}\right)^i t^{i-k}, t \in [t_s, T_F] \end{cases} \\
z^{(k)}(t) &= \begin{cases} (z_{d1} - z_{d0}) \sum_{i=5}^9 \chi_i \frac{i!}{(i-k)!} \left(\frac{1}{T}\right)^i t^{i-k}, t \in [0, t_s) \\ (z_d - z_{d1}) \sum_{i=5}^9 \chi_i \frac{i!}{(i-k)!} \left(\frac{1}{T}\right)^i t^{i-k}, t \in [t_s, T_F] \end{cases}
\end{aligned} \quad (30)$$

where $k = 1, 2, 3, 4$.

Substituting Eq. (26) into Eqs. (28), (29) and (30), the value of the parameter can be obtained.

$$\begin{aligned}
\chi_1 = \chi_2 = \chi_3 = \chi_4 = 0, \chi_5 = 126, \chi_6 = -420, \chi_7 = 540, \chi_8 = -315, \chi_9 = 70 \\
\psi_1 = \psi_2 = \psi_3 = 0, \psi_4 = 35, \psi_5 = -84, \psi_6 = 70, \psi_7 = -20
\end{aligned} \quad (31)$$

Moreover, to prove that the optimal time is available, we write Eq. (30) into the following forms:

$$\begin{cases} \dot{x}(t) = \frac{1}{T} \frac{dx(\rho)}{d\rho} \\ \ddot{x}(t) = \frac{1}{T^2} \frac{d^2x(\rho)}{d\rho^2} \Rightarrow \max |x^{(q)}(t)| = \frac{1}{T^q} \max \left| \frac{d^q x(\rho)}{d\rho^q} \right|, \forall q = 1, 2, 3 \\ x^{(3)} = \frac{1}{T^3} \frac{d^3x(\rho)}{d\rho^3} \end{cases} \quad (32)$$

Using Eqs. (27) and (32), the following results can be obtained:

$$T_F \geq \max \left\{ \frac{1}{v_{1\max}} \max \left| \frac{dx(\rho)}{d\rho} \right|, \left(\frac{1}{a_{1\max}} \max \left| \frac{d^2x(\rho)}{d\rho^2} \right| \right)^{\frac{1}{2}}, \left(\frac{1}{j_{1\max}} \max \left| \frac{d^3x(\rho)}{d\rho^3} \right| \right)^{\frac{1}{3}} \right\} \quad (33)$$

The inequalities for T_F satisfying the y, z direction constraint can be analyzed in the same way. The end time of the trajectory operation satisfies the following inequality:

$$T_F \geq \max \left\{ \frac{1}{v_{i\max}} \max \left| \frac{dx(\rho)}{d\rho} \right|, \left(\frac{1}{a_{i\max}} \max \left| \frac{d^2x(\rho)}{d\rho^2} \right| \right)^{\frac{1}{2}}, \left(\frac{1}{j_{i\max}} \max \left| \frac{d^3x(\rho)}{d\rho^3} \right| \right)^{\frac{1}{3}} \right\}, i = 1, 2, 3, 4 \quad (34)$$

To obtain the minimum value of the ending time, we introduce the idea of dichotomy for the solution. Namely, the following optimal problem is solved.

$$\text{minimize } T_F, \text{ s.t. Eq. (27)} \quad (35)$$

The solution process is implemented in MATLAB, and the specific idea of its programming is shown in Fig. 2.

The initialization is to assign values to the relevant quantities of Eq. (27). T_1 and T_2 are the upper and lower limits of the running time, respectively. ∇ is the allowable error. In summary, the expressions of the optimal time obstacle avoidance trajectory curve

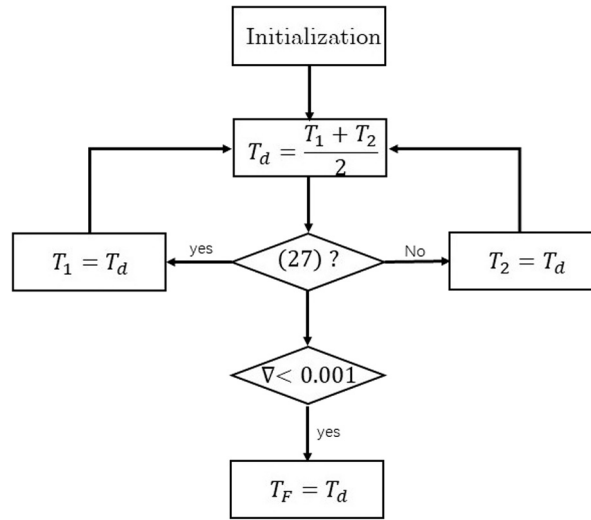


Fig. 2. Dichotomous logic diagram.

are obtained.

$$\begin{aligned}
 x_d(t) &= \begin{cases} (x_{d1} - x_{d0}) \cdot (126\rho^5 - 420\rho^6 + 540\rho^7 - 315\rho^8 + 70\rho^9), t \in [0, t_s] \\ (x_d - x_{d1})(126\rho^5 - 420\rho^6 + 540\rho^7 - 315\rho^8 + 70\rho^9), t \in [t_s, T_F] \end{cases} \\
 y_d(t) &= \begin{cases} (y_{d1} - y_{d0}) \cdot (126\rho^5 - 420\rho^6 + 540\rho^7 - 315\rho^8 + 70\rho^9), t \in [0, t_s] \\ (y_d - y_{d1})(126\rho^5 - 420\rho^6 + 540\rho^7 - 315\rho^8 + 70\rho^9), t \in [t_s, T_F] \end{cases} \\
 z_d(t) &= \begin{cases} (y_{d1} - y_{d0}) \cdot (126\rho^5 - 420\rho^6 + 540\rho^7 - 315\rho^8 + 70\rho^9), t \in [0, t_s] \\ (y_d - y_{d1})(126\rho^5 - 420\rho^6 + 540\rho^7 - 315\rho^8 + 70\rho^9), t \in [t_s, T_F] \end{cases} \\
 y_{0d}(t) &= \begin{cases} y_{0d0} + (y_{0d} - y_{0d0})(35\rho^4 - 84\rho^5 + 70\rho^6 - 20\rho^7), t \in [0, T_F] \\ y_{0d}, t > T_F \end{cases}
 \end{aligned} \quad (36)$$

Thus, the final trajectory of undulation and rotation are obtained through the planning of the y -axis signal at the end of the cantilever and the load coordinate signals by Eqs. (22) and (23). Next, the motion process of the boom is analyzed in detail.

2.4. Obstacle location analysis

In terms of the starting and final positions of the boom movement, it is divided into upward process and downward process. First of all, for the upward trend, the y -axis coordinates of the obstacle are restricted between y_1 and y_2 because the time of encountering the obstacle is calculated from the y -axis coordinates of the end of the cantilever. As in Fig. 3, point $A(x_1, y_1)$ is the projected coordinate of the load on the xoy surface, and point $B(x_2, y_2)$ is the projection of the final coordinate of the load. Generally, the obstacle will only appear between the starting position and the final position. In addition, when the obstacle is located in the orange area, the crane needs to lift over the obstacle before descending to the final position during the rotation. When the obstacle is located in the blue area, the load follows the movement of the cantilever and gradually lifts over the highest point of the obstacle from the starting position to the final position. Similarly, the same is true for the descent process in Fig. 4, which will not be analyzed here.

Remark 1. Even if the locations of obstacles are restricted, this algorithm can realize obstacle avoidance in most areas. And it is well suited in fixed areas. For example, container transportation in ports.

Remark 2. The 3D coordinates of the obstacle can be calibrated by adding the algorithm of binocular vision. Thus, the rotation angle ξ_y and undulation angle ξ_x are obtained, when the load is over the obstacle. Different obstacle avoidance trajectories can be designed by the coordinates of different obstacles.

Remark 3. As expressed in Eq. (36), the obstacle avoidance trajectories $x(t)$, $y(t)$ and $z(t)$ are designed as same order. So that the load moves along a straight line, the oscillation can be reduced effectively.

Remark 4. Considering that in practical applications, the starting position, obstacle position and final position will be different, the trajectories of different positions are formed into a training set to build the neural network. Finally, the control requirement of obstacle avoidance is achieved in real time.

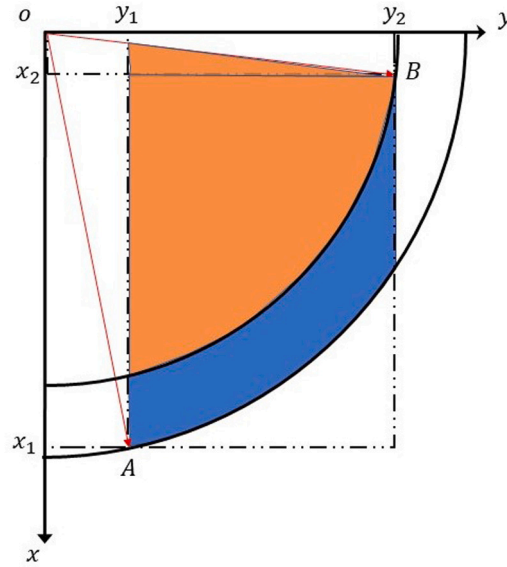


Fig. 3. Projection of the upward process.

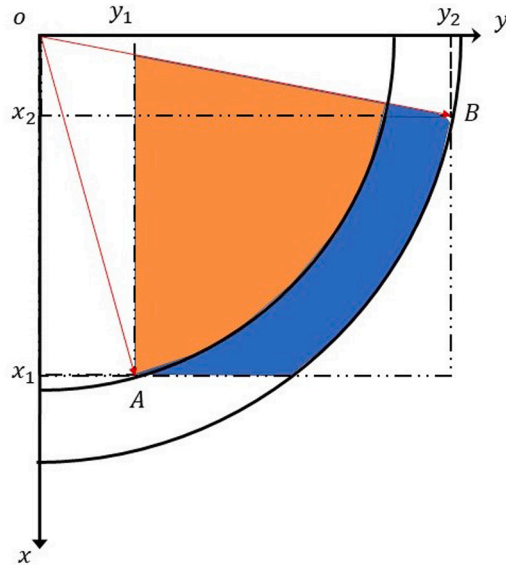


Fig. 4. Projection of the downward process.

3. ANN-based obstacle avoidance trajectory design for real time implementation

This section presents the application of neural networks in the design of real-time obstacle avoidance trajectories. With the development of intelligent control, neural networks can be used both for the identification of unknown system models and for the adjustment of controller parameters [36], etc.

Since the traditional trajectory planning method needs to use look-up tables to get the parameters of the trajectory. Although it saves computation time, it also cannot be realized in real time. Therefore, neural network is introduced to train the parameters of multiple trajectories and predict the parameters of obstacle avoidance trajectories. And the collected input and output data are used for training as shown in Table 2. The ANN constructs a nonlinear mapping, where, ξ_{30} and ξ_{40} are the starting positions of the cantilever. ξ_x and ξ_y are the boom undulation and rotation angles obtained from the 3D coordinates of the obstacle. ξ_{3d} and ξ_{4d} are the undulation and rotation angles of the final position. The first ten samples are trained for different starting positions. The middle ten samples are trained for different obstacle positions. The last samples have different final positions. The angular variations of these samples are adapted to the performance of the crane on the experimental platform. Thus, obstacle avoidance

Table 2
Neural network training set.

Sample No.	ξ_{30} [deg]	ξ_x [deg]	ξ_{3d} [deg]	ξ_{40} [deg]	ξ_y [deg]	ξ_{4d} [deg]	t_s (s)	T_F (s)
1	41	30	35	20	30	35	4.4346	11.7935
2	42	30	35	20	30	35	4.7735	13.3797
3	43	30	35	20	30	35	5.1120	15.2891
4	44	30	35	20	30	35	5.4503	17.7320
5	45	30	35	20	30	35	5.7881	19.7790
6	45	30	35	19	30	35	5.8655	16.7447
7	45	30	35	18	30	35	5.9377	14.9366
8	45	30	35	17	30	35	6.0054	13.9032
9	45	30	35	16	30	35	6.0690	13.2227
10	45	30	35	15	30	35	6.1288	12.7375
11	45	37	45	15	30	45	4.0319	9.1506
12	45	38	45	15	30	45	3.7311	8.2739
13	45	39	45	15	30	45	3.5471	7.6939
14	45	40	45	15	30	45	3.5738	7.5895
15	45	41	45	15	30	45	3.6098	7.5122
16	45	40	45	15	25	45	2.9535	7.4827
17	45	40	45	15	26	45	3.0674	7.4615
18	45	40	45	15	27	45	3.1920	7.4793
19	45	40	45	15	28	45	3.3195	7.5119
20	45	40	45	15	29	45	3.4469	7.5395
21	40	50	60	10	20	30	3.4219	7.0510
22	40	50	61	10	20	30	3.4417	7.1334
23	40	50	62	10	20	30	3.4607	7.2127
24	40	50	63	10	20	30	3.4790	7.2894
25	40	50	64	10	20	30	3.4967	7.3632
26	40	50	64	10	20	31	3.5571	7.6172
27	40	50	64	10	20	32	3.6150	7.8655
28	40	50	64	10	20	33	3.6722	8.1079
29	40	50	64	10	20	34	3.7270	8.3447
30	40	50	64	10	20	35	3.7802	8.5757

trajectory planning can be performed for any obstacle that is within the limitation area. This is done under the condition that the starting position, obstacle position and final position can be measured.

As shown in Fig. 5, the structure of neural network is used in this paper. It has 6 neurons in the input layer, 10 neurons in the hidden layer, and the output layer contains 2 neurons. The neurons in each layer are connected by a weight parameter. a , b and c denote the individual neurons in the input layer, hidden layer and output layer, respectively.

The actual output of the hidden layer and the actual output of the output layer can be expressed by the following equations:

$$Y_b = \text{sigmoid}(\sum_{a=1}^6 X_a W_{ab} - \Delta_b) \quad (37)$$

$$Y_c = \text{sigmoid}(\sum_{b=1}^{10} X_b W_{bc} - \Delta_c) \quad (38)$$

where sigmoid is the activation function. Δ_b is the threshold deviation of the hidden layer connected to fixed neuron -1 . Δ_c is the threshold deviation of the output layer.

In this paper, we use Bayesian regularization to train neural networks. Bayesian regularization can produce good generalization for difficult, small or noisy data sets. Also, The Bayesian regularization method for training neural networks aims to find the weights and biases by minimizing the value of the mean squared error (MSE). The network mapping is constructed to reduce the over-fitting of the training set parameters and is suitable for generalization applications with multiple obstacle angles. The value of the MSE is calculated for each iteration of the neural network. The formula for the MSE is as follows:

$$P = \frac{1}{2A} \sum_{s=1}^A \sum_{e=1}^B (Y_{de}(s) - Y_e(s))^2 \quad (39)$$

where A and B represent the number of samples in the training set and the number of output neurons respectively. $Y_d(s)$ and $Y_e(s)$ represent the expected and actual output values of the s th sample at the e th layer neuron of the output layer.

The constructed neural network was trained by randomly selecting three-fourths of the collected data (in Table 2) as training data and numbering 1, 5, 10, 15, 20, 25, and 30 as the test set. As shown in Fig. 6, the trained neural network solves the MSE minimization problem and achieves a mean squared difference value close to 0. It indicates that the neural net is converged.

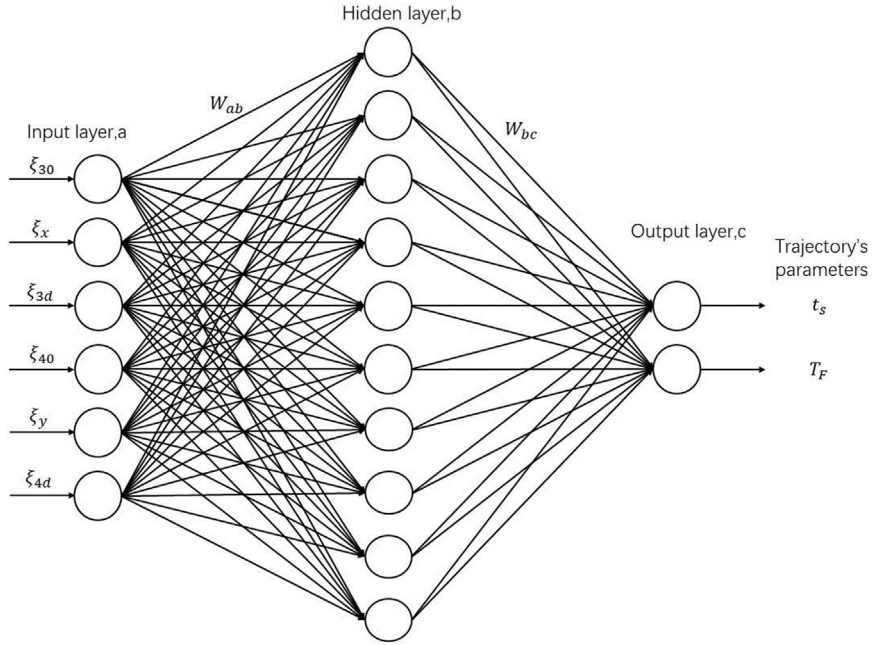


Fig. 5. Structure of the ANN.

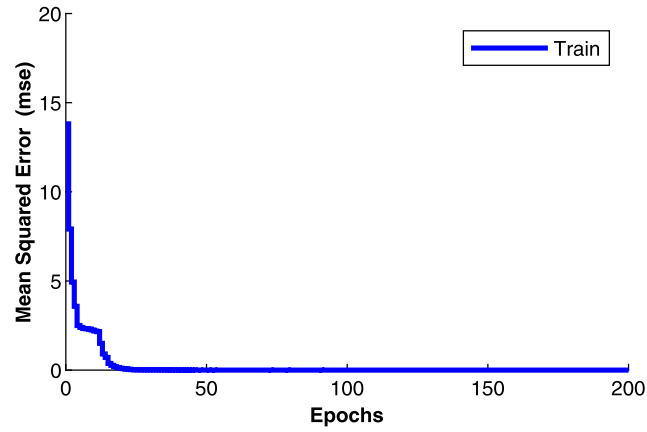


Fig. 6. Relationship between epoch and the MSE during the training process.

Then, the weights and deviations involved are presented as follows:

$$W_{ab}^T = \begin{bmatrix} 1.1685 & -2.8607 & 1.0121 & -1.088 & -0.2592 & -0.2245 \\ -0.2812 & 1.5572 & 0.4364 & 1.9406 & -0.0668 & 0.0247 \\ -0.6661 & -0.7265 & -0.505 & 0.0431 & -0.1002 & 0.1111 \\ -0.1849 & -0.1381 & 0.1479 & -0.1494 & -0.1897 & -0.2070 \\ -0.1761 & 0.0582 & -0.6368 & -0.0103 & -0.0924 & 0.0761 \\ -0.1295 & 1.3425 & 0.3377 & 0.2982 & 0.0799 & 0.3595 \\ -0.2354 & -0.2198 & 0.1508 & -0.1946 & -0.2088 & -0.0660 \\ -0.3304 & -0.3188 & 0.1720 & -0.2577 & -0.1976 & 0.0904 \\ 0.2602 & 0.0342 & -0.1958 & 0.3829 & 0.6558 & -0.2865 \\ -1.1939 & 1.3142 & -0.9464 & -0.2940 & -0.0005 & -0.4814 \end{bmatrix}$$

$$W_{bc}^T = \begin{bmatrix} 1.8809 & 0.4691 & -0.3725 & -0.4825 & 0.3608 & 1.0167 & -0.5595 & -0.7493 & 0.6827 & 1.7020 \\ 1.1511 & 1.6397 & 0.8633 & -0.0605 & 0.2852 & 0.8703 & 0.0258 & 0.1261 & 0.6552 & -0.4403 \end{bmatrix}$$

$$\Delta_b^T = \begin{bmatrix} -1.0536 & 0.2866 & 0.1673 & -0.0838 & 0.2560 & -0.6099 & -0.0164 & 0.0482 & -0.3572 & 0.9924 \end{bmatrix}$$

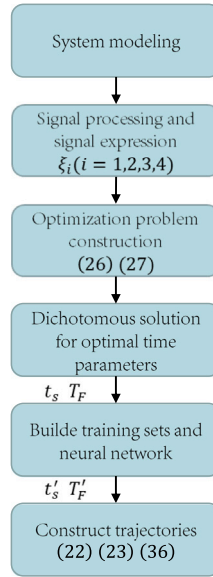


Fig. 7. Algorithm implementation steps.

Table 3
Prediction errors.

Sample No.	1	5	10	15	20	25	30
t_s	4.4346	5.7881	6.1288	3.6098	3.4469	3.4967	3.7802
t'_s	4.4491	5.7736	6.1159	3.8305	3.4486	3.4969	3.7799
ϵ	0.3273%	0.2506%	0.2105%	6.1137%	0.0501%	0.0069%	0.0070%
T_F	11.7935	19.7790	12.7375	7.5122	7.5395	7.3632	8.5757
T'_F	12.6274	19.2419	12.8234	7.9742	7.5544	7.3640	8.5750
ϵ	7.0717%	2.7153%	0.6750%	6.1505%	0.1987%	0.0117%	0.0011%

$$\Delta_c^T = [0.2895 \quad 0.2557] \quad (40)$$

The performance of the neural network is evaluated by the following three data parameters, which include relative error ϵ_i , prediction accuracy ϕ and coefficient of determination η .

$$\begin{aligned} \epsilon_i &= \frac{|t'_i - t_i|}{t_i} * 100\% \\ \phi &= 100\% - \frac{1}{n} \sum_{i=1}^n \frac{|t'_i - t_i|}{t_i} \times 100\% \\ \eta &= 1 - \frac{\sum_{i=1}^n (t'_i - t_i)^2}{\sum_{i=1}^n (t'_i - T)^2} \end{aligned} \quad (41)$$

where t'_i is the time predicted by the neural network and t_i is the real time calculated by the dichotomous method. n is the number of samples involved in the training. And its value is 7. The relative errors of the predicted and actual values are shown specifically in Table 3. t_s and T_F have maximum error of 6.1137% and 7.0717%, respectively. The value of prediction accuracy for t_s and T_F are 99% and 97.59%. It indicates that the constructed neural network mapping have good generalization performance. The coefficients of determination for t_s and T_F are 99.36% and 99.03%, respectively. If the training set of the neural network is continuously increased, the predicted values of the neural network will be closer to the actual values. However, as a method of predicting parameters, there must be an bias between the real value and the predicted value. The best result can only make the biases infinitely close to 0. However, the error will not affect the obstacle avoidance function of the method proposed in this paper because the time only represents how fast the cantilever encounters an obstacle. In summary, the constructed neural network has high accuracy and small relative error. And it can be used for real-time obstacle avoidance trajectory planning of variable obstacle locations.



Fig. 8. Experimental equipment.

Remark 5. From the above results and Fig. 7, we give the following steps to describe the design procedure of the proposed method in this paper:

Step 1: The 3D coordinate signals of the single pendulum rotary crane model are first analyzed. Then both derivable and non-derivable state variables shown in Eqs. (20), (21), (24) and (25) are represented by the coordinate signals, respectively.

Step 2: A series of constraint equations shown in Eq. (26) are established to achieve the control requirements of obstacle avoidance, localization and pendulum elimination. Taking into account the physical constraints of the actual crane operation, the upper limit values shown in Eq. (27) are set. Finally, the proposed constraint equations are solved by the dichotomous method. And the optimal time parameters are substituted into the designed obstacle avoidance trajectory. At the same time, the obstacle avoidance region is analyzed. The obstacle avoidance motion is divided into the upward process and the downward process.

Step 3: Considering the different positions of the obstacles and the starting and final positions of the cantilever, a neural network mapping is established shown in Fig. 5 to obtain the optimal time parameters for different obstacle avoidance trajectories. Eventually, by entering the starting and final positions of the cantilever and the coordinates of the obstacle, the optimal time trajectory for obstacle avoidance can be generated for real time.

4. Experimental implementation and data analysis

In this section, we compared the proposed method with existing methods by satisfying the obstacle avoidance function. This part is divided into three points to be developed. The first point is the introduction of the hardware experimental platform. Then the comparison control method introduced in this paper is given. Finally, a detailed analysis of the experimental data is presented. It is worth mentioning that the data of all experiments are not in the training set of the neural network, so it is verified that the ANN has good generalization performance.

4.1. Experimental equipment

In order to verify the superior performance of the proposed method, we designed the following experimental platform for a rotating crane as shown in Fig. 8, in which the hardware part consists of two angle encoders to measure the swing angle of the load, a DC motor to control the heave and rotation of the rotary crane, a motion control board and a PC unit. The data collected by the encoder is transmitted to the PC through the motion control board. Finally, the data and the program are processed by software, and the control signal is outputted to drive the motor after real-time calculation using Matlab/Simulink, and a sampling interval of 5 ms is set.

The parameters of the experimental platform are as follows:

$$\begin{aligned}
 m &= 0.2 \text{ kg}, M_l = 7.9 \text{ kg}, M_t = 10 \text{ kg} \\
 L &= 0.55 \text{ m}, L_1 = 0.45 \text{ m}, l = 0.15 \text{ m}, g = 9.8 \text{ m/s}^2 \\
 f_{31} &= 4.4, f_{32} = -0.5, f_{41} = 4.3, f_{42} = -0.6, \epsilon = 0.4.
 \end{aligned}$$

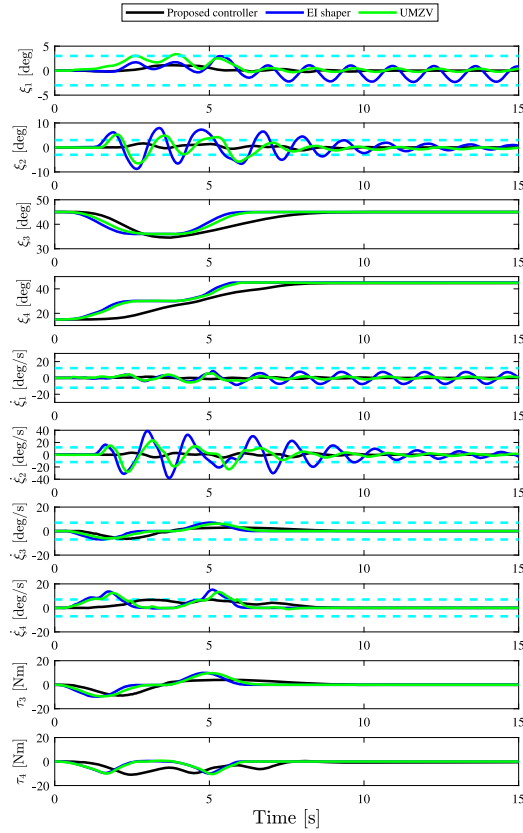


Fig. 9. Comparative experimental results.

In addition, the following starting position, final position and obstacle position are set. We get the parameters of obstacle avoidance trajectory by neural network as $t_s = 4.3228$ s, $T_F = 10.0656$ s.

$$\begin{aligned}\xi_{30} &= 45 \text{ [deg]}, \xi_x = 36 \text{ [deg]}, \xi_{3d} = 45 \text{ [deg]} \\ \xi_{40} &= 15 \text{ [deg]}, \xi_y = 30 \text{ [deg]}, \xi_{4d} = 45 \text{ [deg]}\end{aligned}\quad (42)$$

The restrictions we set on the signals during the design of the obstacle avoidance trajectory are as follows:

$$\begin{aligned}v_{i \max} &= 0.5 \text{ m/s}, a_{i \max} = 0.5 \text{ m/s}^2 \\ j_{i \max} &= 0.5 \text{ m/s}^3, i = 1, 2, 3, 4 \\ \xi_{1 \max} &= 3 \text{ [deg]}, \xi_{2 \max} = 3 \text{ [deg]} \\ \dot{\xi}_{1 \max} &= 12 \text{ [deg/s]}, \dot{\xi}_{2 \max} = 12 \text{ [deg/s]} \\ \dot{\xi}_{3 \max} &= 7 \text{ [deg/s]}, \dot{\xi}_{4 \max} = 7 \text{ [deg/s]} \\ \ddot{\xi}_{3 \max} &= 40 \text{ [deg/s}^2], \ddot{\xi}_{4 \max} = 40 \text{ [deg/s}^2]\end{aligned}\quad (43)$$

After accurate calculation, we can obtain the complete optimal time obstacle avoidance trajectory, which can ensure that the size of the state variables satisfies the above constraints. We track the trajectory by the PD controller. The specific expressions are as follows:

$$\begin{aligned}\tau_3 &= -k_{11}(\xi_3 - \xi_{3S}) - k_{12}(\dot{\xi}_3 - \dot{\xi}_{3S}) - g(0.5M_I L + mL - 0.5M_I L_1)\sin(\xi_3) \\ \tau_4 &= -k_{21}(\xi_4 - \xi_{4S}) - k_{22}(\dot{\xi}_4 - \dot{\xi}_{4S})\end{aligned}\quad (44)$$

where $k_{11} = 190$, $k_{12} = 25$, $k_{21} = 122$, $k_{22} = 15$, ξ_{3S} and ξ_{4S} are the generated obstacle avoidance curve. The last term of τ_3 is the gravity compensation term for the cantilever. The above data were used in all experiments.

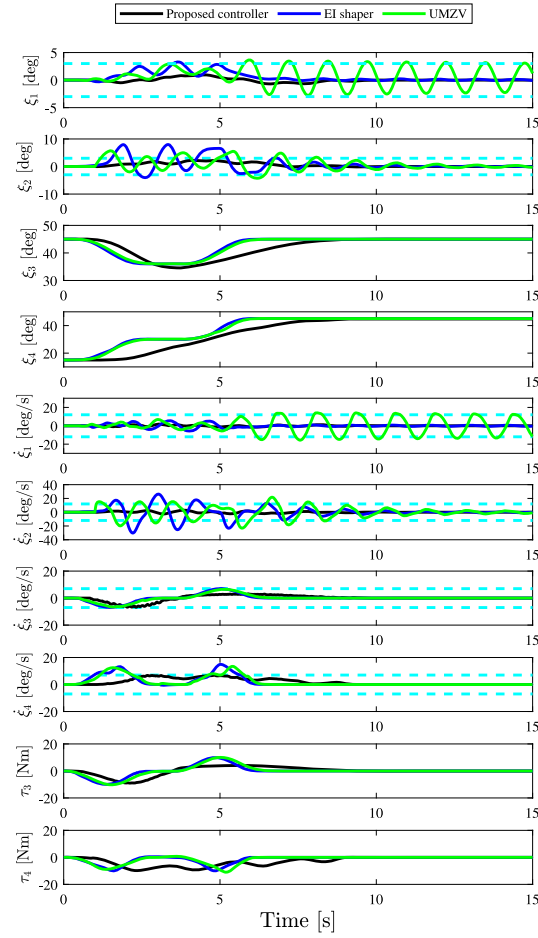


Fig. 10. Experimental results with $m = 0.2$ [kg], $l = 0.25$ [m].

4.2. Comparison experiments

In order to make the control method of comparison achieve the control objective of obstacle avoidance, the following S-shaped trajectory is designed.

$$\xi_3^* = \begin{cases} (\xi_x - \xi_{30})\left(\frac{t}{t_f} - \frac{\sin(\frac{2\pi t}{t_f})}{2\pi}\right) + \xi_{30}, & t \in [0, t_f) \\ \xi_x, & t \in [t_f, t^*) \\ (\xi_{3d} - \xi_x)\left(\frac{t-t^*}{t_f} - \frac{\sin(\frac{2\pi(t-t^*)}{t_f})}{2\pi}\right) + \xi_x, & t \in [t^*, t^* + t_f) \\ \xi_{3d}, & t \in [t^* + t_f, T_{end}] \end{cases} \quad (45)$$

$$\xi_4^* = \begin{cases} (\xi_y - \xi_{40})\left(\frac{t}{t_f} - \frac{\sin(\frac{2\pi t}{t_f})}{2\pi}\right) + \xi_{40}, & t \in [0, t_f) \\ \xi_y, & t \in [t_f, t^*) \\ (\xi_{4d} - \xi_y)\left(\frac{t-t^*}{t_f} - \frac{\sin(\frac{2\pi(t-t^*)}{t_f})}{2\pi}\right) + \xi_y, & t \in [t^*, t^* + t_f) \\ \xi_{4d}, & t \in [t^* + t_f, T_{end}] \end{cases} \quad (46)$$

For a comprehensive consideration of crane motor performance, t_f is set to 2.5 s and $t^* = 3.5$ s. In addition, we use the EI shaper proposed in [37] and the Unity-Magnitude Zero vibration (UMZV) shaper trajectory planning method in [38] as comparison controllers. Similarly, the above input S-curve is tracked by the PD controller. The parameters of the PD controller are selected as follows.

$$k_{11} = 250, k_{12} = 12, k_{21} = 136, k_{22} = 10. \quad (47)$$

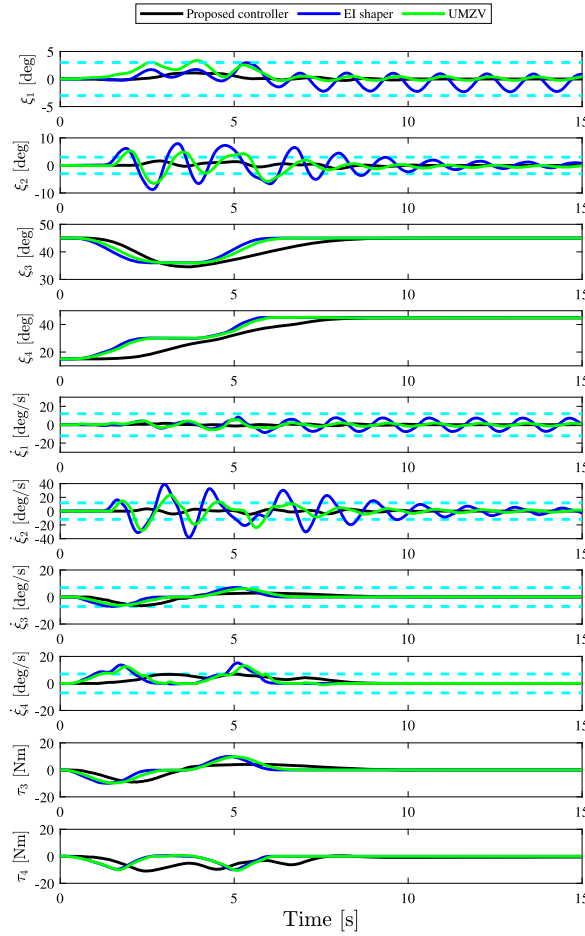


Fig. 11. Experimental results with $m = 0.2$ [kg], $l = 0.37$ [m].

As shown in Fig. 9, the load pendulum angle ξ_1 , ξ_2 and pendulum angle velocity $\dot{\xi}_1$, $\dot{\xi}_2$, the boom undulation angle ξ_3 and rotation angle ξ_4 and their velocity amount $\dot{\xi}_3$, $\dot{\xi}_4$ and the force of the controller τ_3 , τ_4 are given for the proposed and compared methods. As can be seen in the figure, the state variables ξ_3 , ξ_4 and the corresponding speed signals $\dot{\xi}_3$, $\dot{\xi}_4$ can be limited to the set range (blue dashed line in the figure). Therefore, the proposed obstacle avoidance trajectory method can play a role in protecting the motor and limiting the force output of the motor by setting different upper limits. Similarly, the load swing angle ξ_1 , ξ_2 and its angular velocity $\dot{\xi}_1$, $\dot{\xi}_2$ also satisfy the set constraints to realize the load swing elimination of the crane in the operation process. Because there is no acceleration sensor on the experimental platform, the experimental results of acceleration curves are not available in the figure. Since the initial value of the encoder of the heave motor is set to 0. So even if the gravity of the boom is compensated, the force output of the heave motor starts from 0.

Although the EI shaper and UMZV shaper can realize the obstacle avoidance function. However, their obstacle avoidance trajectories are obtained through several experiments, which are not as accurate and convenient as the obstacle avoidance trajectories calculated by the proposed method. Moreover, the swing angle ξ_1 of EI shaper and UMZV shaper are enlarged by 150.82% and 146.01% compared with the set constraints. Also, ξ_2 is enlarged by 230.92% and 242.30%. The comparison methods are not limited by specific constraints in terms of the angular velocity of the load swing angle. At the same time, the residual oscillation of the radial swing angle is not effectively suppressed.

4.3. Robustness analysis

This section focuses on two aspects to verify the robustness of the proposed method. The first part varies the rope length of the load. Although the rope length of the load is varied, the time to encounter the obstacle is obtained by the cantilever y-axis coordinates, so the time parameter of the obstacle avoidance trajectory does not change. The second part of the experiment is validated for loads of different masses.

- Suspended rope length l changes.

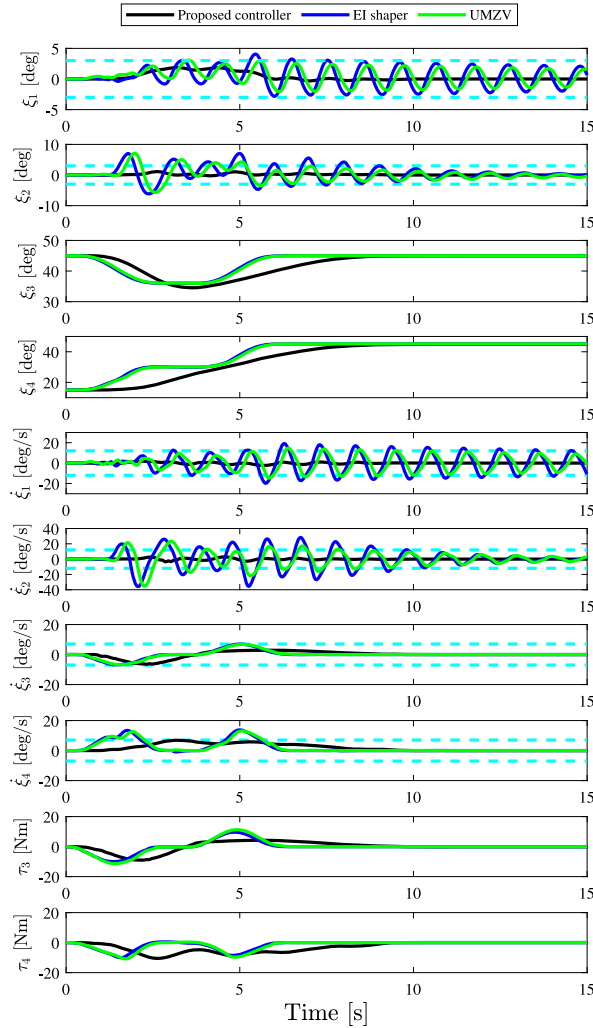


Fig. 12. Experimental results with $m = 0.1$ [kg], $l = 0.15$ [m].

Assuming that the other parameters of the system remain unchanged, modify the length of the rope from 0.15 m to 0.25 m (as shown in Fig. 10) and 0.37 m (as shown in Fig. 11).

- Suspended load mass m changes.

Assuming that the other parameters of the system remain unchanged, modify the mass of the load from 0.2 kg to 0.1 kg (as shown in Fig. 12) and 0.5 kg (as shown in Fig. 13).

From Figs. 10–13, it can be seen that the state variables of the proposed method fluctuate within the set constraints even if the parameters of the system change. It indicates that the designed trajectory not only achieves the requirements of obstacle avoidance, but also has certain robustness to the crane with uncertain parameters. Moreover, the designed trajectory is tracked by the PD controller, and this method is easy to implement in engineering. From the information of the swing angle of the proposed trajectory, the swing amplitude is small and there is almost no residual swing. And the load swing can be effectively suppressed within the calculated optimal end time T_F . The force of the proposed method is also relatively gentle, and there is no effect of jitter on the load. In summary, through experimental verification, the nonlinear obstacle avoidance trajectory planning method designed in this paper can realize the obstacle avoidance by neural network in real time and can meet the superior control performance with different physical constraints.

5. Conclusion

For the nonlinear rotary crane system, the dynamics model of the load was modeled and analyzed deeply. Also, the analysis process was not linearized. Then, trajectories were designed for the control requirements of obstacle avoidance. Next, the optimization problem was solved with the idea of dichotomy. And the results constituted the training set of the neural network.

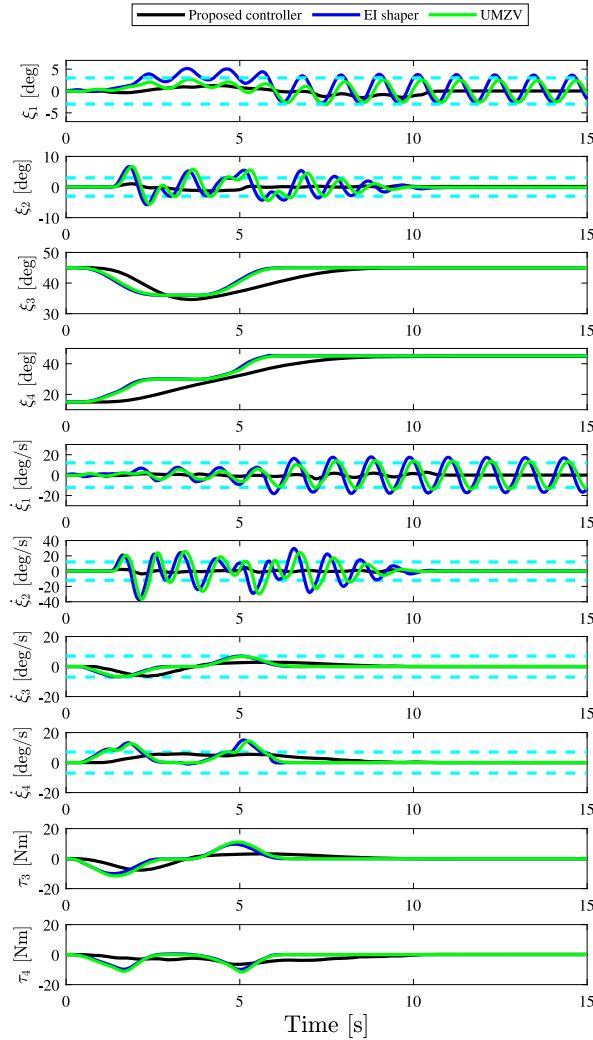


Fig. 13. Experimental results with $m = 0.5$ [kg], $l = 0.15$ [m].

Finally, the mapping relationship was constructed by the neural network to realize the real-time calculation of optimal time trajectory planning. In practice, this not only reduces calculation time but also enhances the efficiency of crane transportation. The generalization analysis of the neural network proved the feasibility of the neural network mapping. In addition, this method can meet the control requirements of nonlinear rotating crane systems with different physical constraints.

However, the algorithm has certain limitations. In the analysis of obstacle locations, the proposed method has some blind spots for the obstacle avoidance area. Similarly, the effect of external disturbances and model parameter changes on the system is not considered in this paper. Therefore, our future work will focus on the following directions:

1. In order to make the proposed algorithm more widely applicable, we will further analyze the effect of external disturbances and model parameter changes.
2. We will analyze the obstacle avoidance of rotary crane in all obstacle areas.
3. We will also study of nonlinear control methods for a class of underactuated systems.

Declaration of competing interest

The authors declare that they have no known competing financial interests or personal relationships that could have appeared to influence the work reported in this paper.

Data availability

Data will be made available on request.

Acknowledgment

This work is supported by the National Natural Science Foundation of China under Grant 61703202.

References

- [1] L. Ramli, Z. Mohamed, et al., Control strategies for crane systems: A comprehensive review, *Mech. Syst. Signal Process.* 95 (2017) 1–23.
- [2] T. Yang, N. Sun, et al., Neural network-based adaptive anti-swing control of an underactuated ship-mounted crane with roll motions and input dead zones, *IEEE Trans. Neural Netw. Learn. Syst.* 31 (3) (2020) 901–914.
- [3] M. Zhang, X. Ma, et al., A partially saturated adaptive learning controller for overhead cranes with payload hoisting/lowering and unknown parameters, *Nonlinear Dynam.* 89 (3) (2017) 1779–1791.
- [4] W. He, S. Zhang, et al., Adaptive control of a flexible crane system with the boundary output constraint, *IEEE Trans. Ind. Electron.* 61 (8) (2014) 4126–4133.
- [5] M. Zhang, X. Ma, et al., Adaptive tracking control for double-pendulum overhead cranes subject to tracking error limitation, parametric uncertainties and external disturbances, *Mech. Syst. Signal Process.* 76–77 (2016) 15–32.
- [6] M. Zhang, Y. Zhang, et al., An enhanced coupling PD with sliding mode control method for underactuated double-pendulum overhead crane systems, *Int. J. Control Autom. Syst.* 17 (6) (2019) 1579–1588.
- [7] L.A. Tuan, Fractional-order fast terminal back-stepping sliding mode control of crawler cranes, *Mech. Mach. Theory* 137 (2019) 297–314.
- [8] D. Chwa, Sliding-mode-control-based robust finite-time anti-sway tracking control of 3-D overhead cranes, *IEEE Trans. Ind. Electron.* 64 (8) (2017) 6775–6784.
- [9] M. Zhang, X. Jing, et al., Disturbance employment-based sliding mode control for 4-DOF tower crane systems, *Mech. Syst. Signal Process.* 161 (2021) 107946.
- [10] H. Ouyang, Z. Tian, et al., Load swing rejection for double-pendulum tower cranes using energy-shaping-based control with actuator output limitation, *ISA Trans.* 101 (2020) 246–255.
- [11] N. Sun, Y. Fang, et al., Energy coupling output feedback control of 4-DOF underactuated cranes with saturated inputs, *Automatica* 49 (5) (2013) 1318–1325.
- [12] H. Ouyang, B. Zhao, et al., Enhanced-coupling nonlinear controller design for load swing suppression in three-dimensional overhead cranes with double-pendulum effect, *ISA Trans.* 115 (2021) 95–107.
- [13] D. Wang, H. He, et al., Intelligent optimal control with critic learning for a nonlinear overhead crane system, *IEEE Trans. Ind. Inf.* 14 (7) (2018) 2932–2940.
- [14] J. Smoczek, J. Szpytko, Particle swarm optimization-based multivariable generalized predictive control for an overhead crane, *IEEE/ASME Trans. Mechatronics* 22 (1) (2017) 258–268.
- [15] N. Sun, Y. Wu, et al., An energy-optimal solution for transportation control of cranes with double pendulum dynamics: Design and experiments, *Mech. Syst. Signal Process.* 102 (2018) 87–101.
- [16] Q. Wu, X. Wang, et al., Improved time optimal anti-swing control system based on low-pass filter for double pendulum crane system with distributed mass beam, *Mech. Syst. Signal Process.* 151 (2021) 107444.
- [17] S. Kimmmerle, M. Gerds, et al., An optimal control problem for a rotating elastic crane-trolley-load system, *IFAC-PapersOnLine* 51 (2) (2018) 272–277.
- [18] L. Ramli, Z. Mohamed, et al., A neural network-based input shaping for swing suppression of an overhead crane under payload hoisting and mass variations, *Mech. Syst. Signal Process.* 107 (2018) 484–501.
- [19] H. Saeidi, M. Naraghi, et al., A neural network self tuner based on input shapers behavior for anti sway system of gantry cranes, *J. Vib. Control* 19 (13) (2013) 1936–1949.
- [20] B. Benhellal, M. Hamerlain, et al., Decoupled adaptive neuro-interval type-2 fuzzy sliding mode control applied in a 3D crane system, *Arab. J. Sci. Eng.* 43 (6) (2018) 2725–2733.
- [21] M.J. Maghsoudi, L. Ramli, et al., Improved unity magnitude input shaping scheme for sway control of an underactuated 3D overhead crane with hoisting, *Mech. Syst. Signal Process.* 123 (2019) 466–482.
- [22] M.J. Maghsoudi, Z. Mohamed, et al., An optimal performance control scheme for a 3D crane, *Mech. Syst. Signal Process.* 66–67 (2016) 756–768.
- [23] K.L. Sorensen, K. Hekman, et al., Finite-state input shaping, *IEEE Trans. Control Syst. Technol.* 18 (3) (2010) 664–672.
- [24] S.S. Gürlük, Optimal unity-magnitude input shaper duration analysis, *Arch. Appl. Mech.* 77 (1) (2006) 63–71.
- [25] H. Ouyang, X. Xu, et al., Energy-shaping-based nonlinear controller design for rotary cranes with double-pendulum effect considering actuator saturation, *Autom. Constr.* 111 (2020) 103054.
- [26] H. Ouyang, X. Xu, et al., Nonlinear-adaptive-based swing reduction control for rotary cranes with double-pendulum effect considering uncertain parameters and external disturbances, *Autom. Constr.* 126 (2021) 103668.
- [27] T. Yang, N. Sun, et al., Motion trajectory-based transportation control for 3-D boom cranes: Analysis, design, and experiments, *IEEE Trans. Ind. Electron.* 66 (5) (2019) 3636–3646.
- [28] K. Nakazono, K. Ohnishi, et al., Vibration control of load for rotary crane system using neural network with GA-based training, *Artif. Life Robot.* 13 (1) (2008) 98–101.
- [29] T. Yang, H. Chen, et al., Adaptive neural network output feedback control of uncertain underactuated systems with actuated and unactuated state constraints, *IEEE Trans. Syst. Man Cybern.: Syst.* (2021) <http://dx.doi.org/10.1109/TSMC.2021.3131843>, early access.
- [30] T. Yang, N. Sun, et al., Adaptive optimal motion control of uncertain underactuated mechatronic systems with actuator constraints, *IEEE/ASME Trans. Mechatronics* (2022) <http://dx.doi.org/10.1109/TMECH.2022.3192002>, early access.
- [31] T. Yang, N. Sun, et al., Neuroadaptive control for complicated underactuated systems with simultaneous output and velocity constraints exerted on both actuated and unactuated states, *IEEE Trans. Neural Netw. Learn. Syst.* <http://dx.doi.org/10.1109/TNNLS.2021.3115960>, early access.
- [32] Y. Qian, D. Hu, et al., Adaptive neural network-based tracking control of underactuated offshore ship-to-ship crane systems subject to unknown wave motions disturbances, *IEEE Trans. Syst. Man Cybern.: Syst.* 52 (6) (2022) 3626–3637.
- [33] Y. Qian, D. Hu, et al., Programming-based optimal learning sliding mode control for cooperative dual ship-mounted cranes against unmatched external disturbances, *IEEE Trans. Autom. Sci. Eng.* <http://dx.doi.org/10.1109/TASE.2022.3182720>, early access.
- [34] H. Chen, Y. Fang, et al., A novel optimal trajectory planning method for overhead cranes with analytical expressions, in: *Proceedings of the 33rd Chinese Control Conference*, 2014, pp. 7953–7958.
- [35] N. Uchiyama, H. Ouyang, et al., Simple rotary crane dynamics modeling and open-loop control for residual load sway suppression by only horizontal boom motion, *Mechatronics* 23 (8) (2013) 1223–1236.
- [36] L.C. Jain, M. Seera, et al., A review of online learning in supervised neural networks, *Neural Comput. Appl.* 25 (3–4) (2014) 491–509.
- [37] J. Huang, E. Maleki, et al., Dynamics and swing control of mobile boom cranes subject to wind disturbances, *IET Control Theory Appl.* 7 (9) (2013) 1187–1195.
- [38] K.L. Sorensen, K. Hekman, et al., Finite-state input shaping, *IEEE Trans. Control Syst. Technol.* 18 (3) (2010) 664–672.